Eddy Current Testing Instrument for Online Industrial Quality Control

Hugo Zacarias
Electronic Engineer Master Degree
Instituto Superior Técnico
Lisboa, Portugal
hugo.zacarias@tecnico.ulisboa.pt

***Abstract*—Non-destructive testing is one of the most used methods to control the quality and properties of materials, namely in the metal industry. Eddy current testing is an electromagnetic testing method. The principle is to induce an electric current in a conductive material and analyze its response. This allows superficial and depth flaw detection, conductivity measures and more. This work presents the development of a modular instrument that is able to perform online eddy current testing, implement signal detection and classification, operate autonomous and provide monitoring information while being accessed remotely through Ethernet communication. The developed system incorporates eddy current testing front-end modules to analyze the eddy currents response, a processing core to process the data from the front-end ECT modules and allow the remote access functionalities**

Keywords—Non-destructive techniques, eddy current testing, electromagnetic testing method, signal detection, remote access.

I. INTRODUCTION

Non-Destructive testing (NDT) comprises several analysis techniques both used in science and industry. Those allow the evaluation of the properties of a material, object or system, without causing any damage nor permanently change the tested component. Due to this characteristic, these techniques have been adopted by many manufacturers, proving to be a method to save money and time, both in research, maintenance and manufacturing. Some of the most used NDT techniques are visual test, ultrasonic, liquid penetration and electromagnetic.

Eddy Current Testing (ECT) is a non-destructive electromagnetic method used to detect surface or below surface flaws. In this method, a coil (probe) is excited with an alternating electrical current, producing an alternating magnetic field around itself. This field oscillates at the same frequency has the current flowing through the coil. When the probe approaches a conductive material, the magnetic field penetrates the material, generating continuous and circular eddy-currents. The induced currents flowing within the test piece generate a secondary magnetic field, opposite to the primary one. This second magnetic field will affect the primary one, weakening it. By monitoring the resulting magnetic field is possible to detect a flaw in the test piece, has it will change compared to the rest of the piece [1].

ECT can be very useful to measure a large variety of properties, such as the thickness of the coating on the test piece, electrical conductivity, magnetic permeability, corrosion evaluation, distinguish between different alloy compositions, determine the hardness of the test piece and flaw detection. To improve the reliability, or in some cases to be possible to achieve certain measures, enhancement techniques are used. These techniques may include multiple frequencies used to detect flaws in different depths or probes with multiple coils to increase signal to noise ratio (SNR). The advantages of using eddy currents as a non-destructive method is the insensitivity to oils, dust and dielectric materials, the possibility to operate at high temperature range, high speed readings and its reliability. On the other hand, eddy currents testing is limited to materials with electrical conductive properties and unwanted surface variations are sensed. In addition is dependent of flaw orientation and has a limited depth of penetration.

Non-destructive techniques are widely used to reduce production costs, ensure quality control even in non-critical areas, leading for a better quality of the final product and operational readiness. This motivate companies to invest in NDT and employ these methods in the production pipeline. Normal systems use a display close to the ECT device, receiving real-time readings and warnings, has well has a history of the measurements. The device developed in this thesis extend these functionalities, allowing remote access to the ECT device, giving the user the possibility to check the state of the quality control. The system employs multiple instances of an electronic front-end module dedicated to ECT measurements. The processing core should be powerful enough to handle multiple ECT front-end modules and its respective provided data. It should also be able to connect to the internet, in order to provide remote access for the user.

II. STATE OF THE ART

A. Non-Destructive Techniques

Non-destructive testing is one of the most used techniques to inspect, test, evaluate materials, components or monitor discontinuities without destroying the testing peace nor alter its properties.

In comparison, other techniques rely on destroying a lot sampling, a fabricated product piece sacrificed for the required tests. These destructive tests are used to evaluate the physical properties of the material, such has durability, impact resistance, among others. The idea is that in order to achieve a representative sampling, many products have to be destroyed, leading to a decrease in revenue for the company and more time-consuming testing [4].

Eddy current testing is one method of the many NDT methods, relying on electromagnetic testing. Other methods are the magnetic particle testing, liquid penetrant testing, radiographic testing, ultrasonic testing, visual testing, acoustic emission testing, guided wave testing, laser testing methods, leak testing, magnetic flux leakage, neutron radiographic testing, thermal/infrared testing and vibration analysis.

B. Eddy Current

In 1851, Leon Foucault, a French physicist discovered the eddy current phenomenon. His discovery was based on a device that used a copper disk moving in a strong magnetic field, showing that eddy currents are generated when a material moves within an applied field, requiring a greater magnetic force to maintain the same rotation due to eddy current effects [2]. This concept was supported by the Faraday Law that states that a current will flow through a conductor, if an altering magnetic field is applied to it, or if a conductor passes through a magnetic field. In both cases, the conductor must have a closed path where the current may flow.

ECT uses alternating electrical current to energize a coil, creating a time-varying magnetic field. If an electrically conductive material is in proximity to this electromagnetic field, an eddy current will be induced in the material, has Faraday's Law shows in

$$\varepsilon = -\frac{d\phi_B}{dt}. \quad (1)$$

The electromotive force ε is proportional to the time-rate change of the magnetic induction flux density ϕ_B.

The induced eddy current in the test piece will generate a secondary magnetic field that tends to oppose the primary magnetic field, generated by the coil. The interaction between the fields causes a wakening effect on the one generated from the coil, therefore an apparent change in the impedance of the coil, has shown in Figure 1.

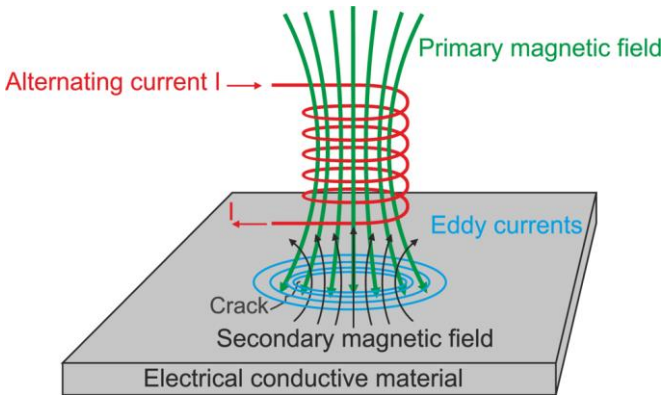

Figure 1 - Eddy current on the test piece (adapted from [1]).

It's possible to monitor the weakening effect on the coil due to how it's characterized by the impedance parameter Z_0, which is a complex number defined as

$$Z_0 = \frac{V_0}{I_0} = R_0 + jX_0 = R_0 + j2\pi fL_0 = |Z|_\phi, \quad (2)$$

which represents the voltage-current ratio (V_0 / I_0) for a single sinusoidal frequency f.

Measuring the coil impedance before approaching the test piece (Z_0) to eddy currents contribution (Z_c), by either monitoring the current or the voltage on the signal, is possible to retrieve specific information such as conductivity and magnetic composition on the test piece [3]. This change of the impedance depends on the distance between the coil and the material, the conductivity and the permeability of the material [4], the surface and subsurface geometry. The presence of a material flaw will disturb or impede induced eddy currents and in response will also change the apparent impedance of the coil [5].

The impedance changes are analyzed in the complex impedance plane. When there is no test piece near the coil sensor, its impedance is a complex value given by

$$Z_0 = R_0 + jX_0, \quad (3)$$

where R_0 is the real part, and jX_0 the imaginary one. $X_0 = 2\pi fL_0$ and it's proportional to the frequency f and the induction coefficient L_0.

Once a conductive material approaches the sensing coil, energized by an altering current, eddy currents will appear on the test piece, creating a secondary field that interacts with the primary one. This interaction will change the sensing coil impedance, given by

$$Z_c = R_c + jX_c, \quad (4)$$

where $X_c = 2\pi fL_c$, being L_c the induction coefficient when a test piece is near the sensing coil.

Once known this value is possible to draw a point in the impedance plane, where the X-axis represents the real part, while the Y-axis the imaginary part, as show in the Figure 2.

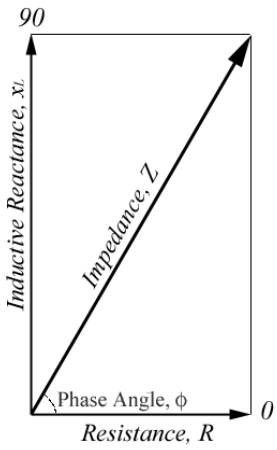

Figure 2 - Complex Impedance plane (adapted from [6]).

The impedance plane diagram is a useful tool to display eddy current data, due to the fact that a variation in the test piece, for instance a crack, will alter the sensing coil impedance, therefore plotting a different result in the complex plane.

To detect flaws in eddy current testing, the use of different frequencies on the inspection is crucial. As (2) demonstrates, if frequency is increased, the imaginary part of the impedance also increases.

There are some issues with ECT, and one of the most important is the depth of penetration. The penetration of the eddy currents is limited due to the skin effect, that is the tendency of an alternating electrical current to become

distributed within the surface of the test piece such that the current density is largest near the surface of the piece and decreases exponentially with greater depths. Considering the current density flowing along X axis, current flux is represented as

$$\vec{J} = J_x(\mathrm{z},\mathrm{t}) * \vec{u_x}, \tag{5}$$

where $\vec{u_x}$ represents the unitary vector along the X axis and $J_x(\mathrm{z},\mathrm{t})$ the magnitude of density current as function of the depth z and time t. The phasor of the density along depth (Z axis) is obtained by

$$J_x(\mathrm{z}) = J_{0,\max} e^{-\frac{z}{\delta}} e^{j(\alpha_0 - \frac{z}{\delta})}, \tag{6}$$

where $J_{0,\max}$ is the maximum current density at surface and z the depth [7]. The depth at which eddy-current density decreases to a level around 37% of its surface value it's the standard penetration depth δ. α_0 represents the phase at $t = 0$ and $z = 0$. $-\frac{z}{\delta}$ is the phase lag, that represents the shift in time between the eddy current response from a disruption on the surface of the test piece and a disruption at some distance below the surface. With it is possible to predict the depth of the flaw.

Extracting the real part from (5), the variation in the current density phase is 1 radian when the distance traveled from the surface is δ as

$$\mathrm{Real}(\mathrm{J}_x(\mathrm{z}) * \mathrm{e}^{jwt}) = \mathrm{J}_{0,\max} e^{-\frac{z}{\delta}} \cos(\omega \mathrm{t} + \alpha_0 - \frac{z}{\delta}). \tag{7}$$

Standard penetration depth can be calculated as in

$$\delta = \sqrt{\frac{2}{\mu\omega\sigma}} \tag{8}$$

where μ is the magnetic permeability, $\omega = 2\pi f$ and σ is the conductivity. According to (8) is possible to identify that the standard penetration depth depends on the magnetic permeability, on the double of the frequency and on the conductivity. In case if any of these variables increase, penetration depth decreases. To illustrate this variation, Table 1 represents the variation in the penetration depth in a copper piece, changing the frequency of the input signal.

Table 1 - Penetration depth in copper using different frequencies (adapted from [8]).

Frequency	Penetration Depth (µm)
60 Hz	8470
10 KHz	660
100 KHz	210
1 MHz	66

Figure 3 also shows the same phenomena, with a graphical approach that shows the importance of higher frequency for a better resolution.

The operational frequency can't be too low, since the test piece thickness must be two or three times the standard depth of penetration to prevent substantial eddy currents from appearing on the other side of the test piece.

Low frequency tests are usually used in the inspection of ferromagnetic materials to compensate their higher permeability and penetrate the test piece. High frequency tests are used when small discontinuities may occur in the near-surface region, ensuring the maximum eddy current flow at the surface.

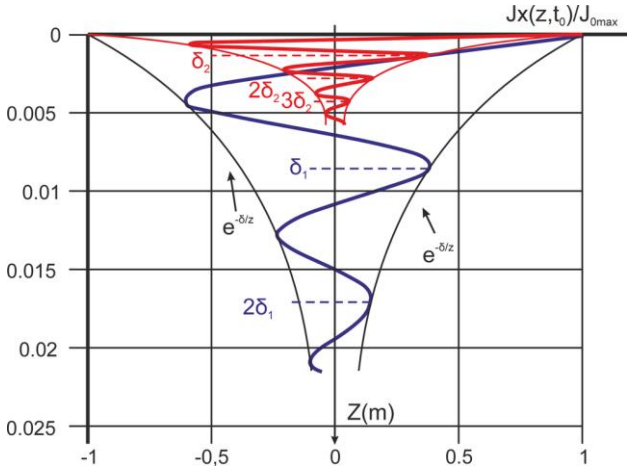

Figure 3 - Electromagnetic field penetration inside pure aluminum at frequencies of 200 Hz and 10 KHz (adapted from [7]).

The band of operating frequencies is selected according to the crack morphology, crack position and skin effect. The sensitivity reaches its maximum value at the optimum frequency. In the case of the test piece having more than one flaw, it can be hard to detect all of them, or even impossible when using only one frequency.

Multi-frequency techniques can operate at two or more frequencies using a composite signal. This type of technique save time and expand the single frequency capabilities, by allowing simultaneous tests, analyze in more detail flaws which have complex shapes or canceling undesired signals, to improve signal-to-noise ratio. The undesirable signal is subtracted to the composite one, reducing noise sources such as probe lift-off, temperature variation and geometrical changes in the test piece.

The excitation frequencies can be applied either simultaneously or sequentially. Simultaneous applications will result in a shorter testing time, but each frequency will have less power compared to a sequential approach. Sequential application allows for increased power per frequency, but when applying a new one the system must have time to reach a steady state before initializing the test [9].

These techniques are usually achieved by combining results at different frequencies in the spatial domain. Combining multi-frequency methods with raster scanning is possible to obtain an image of the impedance or the impedance changes in a two-dimensional (2-D) surface. The acquired images are complex values because impedance itself produces complex data. Authors as Bartels and Fisher have researched a multifrequency eddy current image processing techniques for NDT [10]. The 2-D eddy current testing generate a sequence of complex valued images which are linearly combined to maximize the SNR in beneficial

situations. This technique consisted of a selection of weights for a linear combination of the images as

$$d(\mathrm{x},\mathrm{y}) = \sum_{i=1}^{2N_f} c_i\, f_i(\mathrm{x},\mathrm{y}), \tag{9}$$

where $d(\mathrm{x},\mathrm{y})$ is the linear combination of images, N_f the number of test frequencies.

Extracting the 2-D images is possible to obtain h1, h2 … hN_f to be used in $f1 = real(\mathrm{h1})$, $f2 = imag(\mathrm{h1})$, $f3 = real(\mathrm{h2})$ and so on. Results on this research shown an SNR improvement up to 1100 percent over traditional two-frequency techniques.

Traditional eddy-current systems use a single sinusoidal frequency. These are limited by the depth of penetration of eddy currents. Because of it, traditional systems are useful for analyzing surface up to a few millimeters below surface cracks. To increase the subsurface testing, usually reducing the operational frequency shows improvement, increasing the standard depth of penetration. However, in many situations, SNR is reduced.

In order to improve this factor, Pulsed Eddy Current (PEC) instruments are used, being able to generate square, triangle or a saw tooth waveform. These waveforms have a broad, and theoretically infinite (Figure 4), frequencies, allowing pulsed eddy current techniques to provide more information than the traditional ones. Correlating the data at different frequencies allow to obtain the crack depth.

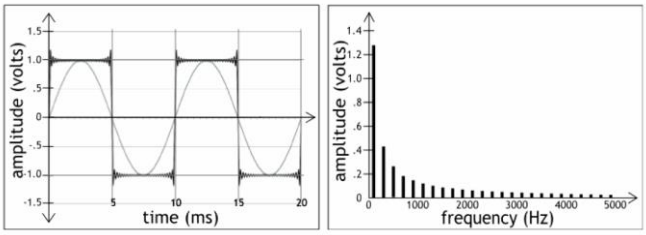

Figure 4 - Twenty-five harmonic square wave frequency response (adapted from [11]).

Usually pulsed eddy current instruments are implemented with two coils, one transmitter and one receiver, or a double-function coil. At the same time, the current driving the transmit coil can be made higher in order to improve the reception SNR.

This technique can be used for both crack detection, but also to accurately characterize the permeability and the conductivity of the test piece [10]. Developed systems that use PEC are able to achieve measurements of thickness at very large lift-off distances (up to 100 mm) [9].

These systems permit the detection of flaws, near the surface and in depth, simultaneously, without the need to change the probe or the operating frequency [12]. Each pulse consists in a continuous sequence of frequencies, especially rich in low-frequency components, providing better sub-surface flaw detection. The deeper a signal penetrates, longer it takes to retrieve information to the probe, therefore each component carries information from different depths.

ECT response data can be analyzed in frequency domain, time domain or both. In time domain analysis the peak amplitude is used to determine the size of the defect, while the time to zero crossing the depth of the flaw as shown in Figure 5. The deeper the flaw in the test piece, longer the time to zero crossing.

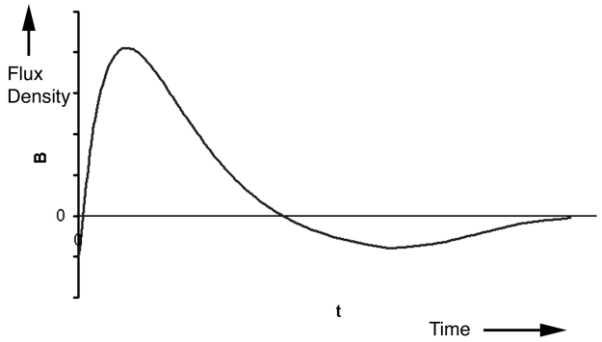

Figure 5. Typical time domain response in pulsed eddy current testing (adapted from [9]).

III. System Achitecture

A. System Hardware Architecture

The proposed system is composed by a processing core, ECT front-end modules and a power supply. The Beaglebone Black is the processing core of the system and is what makes possible the internet connection and remote access with the included Ethernet port. According to the values received from the front-end modules, a response may be applied to a LED, a relay, a buzzer or a display. All the actuators are part of the IO/Alarms module. The processing core needed to be powerful enough to handle multiple ECT front-end modules and its respective provided data, as well as connect to the internet by Ethernet connection.

Four MSP430 from Texas Instruments are used as ECT front-end modules to readout up to four coil elements of a connected probe. The front-ends digital output response is composed by real and imaginary part. They communicate with the processing core through SPI for a fast and reliable connection. This connection will ensure readings from multiple front-end modules and future proof expansion.

The power management module is composed by two stages. The first stage uses DC/DC converters to transform the 20 V DC input voltage into +13.5 V, -13.5V and 5 V. These voltages are then converted into +12 V, -12 V and 3.3 V, respectively, using linear regulators. The +12 V and -12 V are used to drive the operational amplifiers generating or amplifying the probes signals. The processing core uses the 5 V produced by the DC/DC converter for power and the front-end modules use the 3.3 V. The system architecture is present on the Figure 6.

During the process of choosing the right hardware, comparisons between Raspberry Pi2 and Pi3, Beaglebone Black and a BeagleBoard X15 were undertaken. The necessity to connect multiple ECT front-end modules was the main factor to remove the Raspberry modules from the possibilities. Having a parallel communication port alongside multiple SPI pins was the best possible configuration that only the BeagleBoard X15 offered, but the over 200€ cost of this development board made it hard to choose. To round everything, the Beaglebone Black was chosen for the superior number of SPI ports and the larger onboard storage capacity, compared to the Raspberry Pi variants and the more affordable price tag than the BeagleBoard X15.

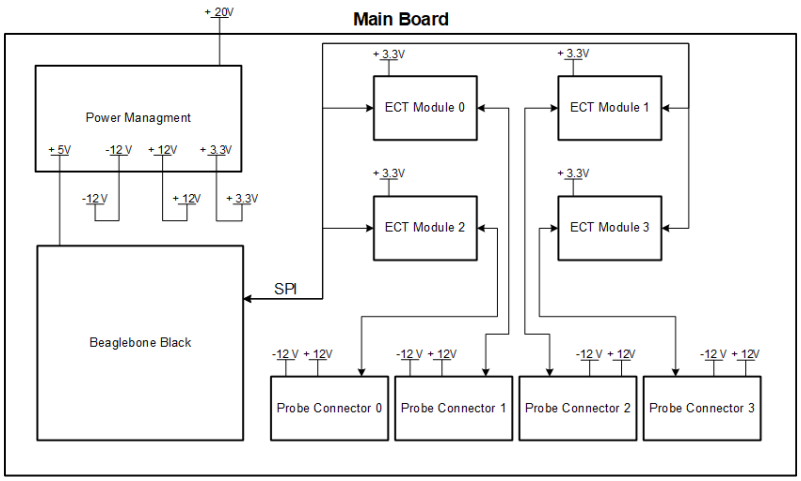

Figure 6 – System Architecture.

The ECT Front-end Modules implement several functionalities, such as probe signaling and calibration, signal processing and storage. The development of the modules' hardware is not credited to the author. Figure 7 shows on of the used prototypes.

These are based on the microcontroller MSP430 FR2355 from Texas Instruments. The 4 SPI channels, internal 12-bit ADC and 6-bit DAC, the up to 24 MHz internal clock and the built-in programmable gain amplifiers (PGAs) were some of the features that lead to choose this microcontroller has a foundation of the eddy current front-end modules.

The sinusoidal and complementary signals, used in the ECT probes, are internally generated using software. This topic is covered on the Software Architecture section. To increase the output current, THS3062 high output operation amplifiers are used, allowing a maximum of 100 mA to be sourced through each channel, while the output voltage maintains ±12 V with 16 Vpp.

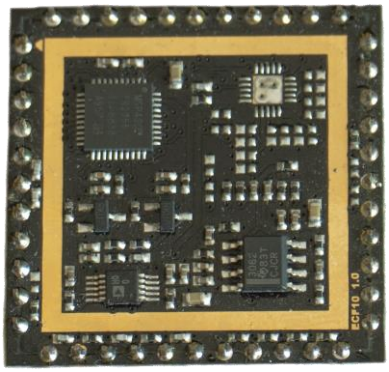

Figure 7 - ECT Front-End Module Layout.

To achieve the required supply voltages, circuitry was necessary. For the first stage, TPS5430 step-down converters from Texas Instruments were used. This component was chosen due to the considerable input voltage range, from 5.5 V up to 36 V, meaning that a different power supply may be used in the future. Another important factor was the necessary 3 A continuous output current to power the Beaglebone Black. The different voltages were based on the schematic present on Figure 8. Analyzing the schematic, is possible to identify a buck converter, where the output voltage provides the control to the TPS5430 through the VSENSE connection. The feedback network voltage signal is compared to a reference voltage value, which, depending on the value, will actuate on the PWM controller, changing the duty cycle of the FET switch on state. Overall, it works as a switch, controlled by the VSENSE signal, providing the desired output voltage.

Analyzing the circuit, and assuming that it is working in continuous mode, when the FET Switch is closed, the current will flow through the inductor, increasing at a rate of

$$\frac{d_i}{d_t} = \frac{V_{in} - V_{out}}{L}, \tag{10}$$

where

$$V_L = V_{in} - V_{out}, \tag{11}$$

is the voltage drop on the inductor. When the switch is opened, the current flow must maintain the same direction, therefore, it goes through the inductor, into the load, and back to the inductor passing the diode. With this, the inductor voltage is reverted in order to keep the current

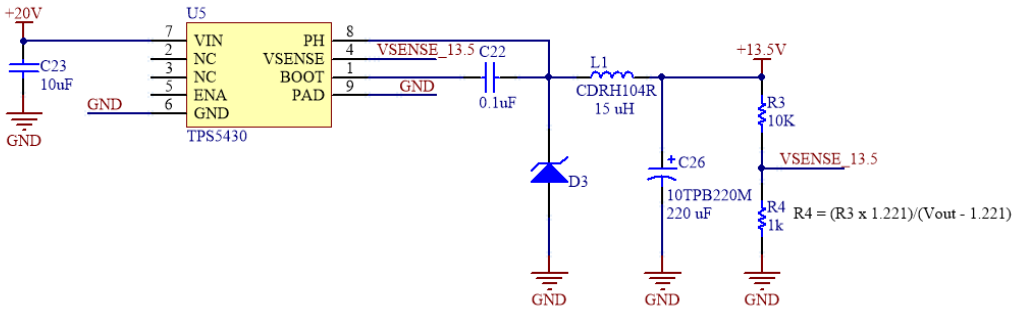

Figure 8 – Step-Down Converter Schematic for +13.5 V.

flow, being

$$V_L = -V_{out}. \quad (12)$$

The input capacitor C23 is decoupling the input voltage from the rest of the circuit, while both the capacitor C26 and inductor L1 are creating a necessary output filter.

Different output voltages can be obtained by changing the R4 resistor value as

$$R_4 = \frac{R_3 \times 1.221}{V_{Out} - 1.221}, \quad (13)$$

where R_3 is a fixed value of 10 kΩ and V_{Out} the desired output voltage.

To obtain -13.5 V a slightly different circuitry was used, as show on Figure 9. Compared to the previous schematic, the output voltage and ground are switched, making the circuitry behave in a very interesting way in order to achieve negative voltages. When the FET switch on the TPS5430 is closed, the current flows through the inductor, all the way to the ground terminal. Whereas the output capacitor delivers the output current load, maintaining a negative value. When the switch is opened, the diode becomes direct polarized, the current from the inductor splits between the capacitor and the load, charging the capacitor and maintaining the negative value at the load. This charge up the capacitor, inverting the voltage on the terminals of the inductor.

Similarly, to the previous schematic, the voltage divider defines the output voltage, having an impact on the duty cycle of the internal TPS5430 switch. The 20 V input voltage is used to achieve a negative voltage using a buck DC-DC converter. Any step-down DC-DC converter can be used as an inverter, simply by changing the label of some pins. The V_{out} pin is labelled as GND in the inverter, and the GND pin as $-V_{out}$. But there are some limitations using this approach. For instance, the voltage difference between the input and output voltages cannot be higher than the buck DC-DC converter's maximum operating input voltage. Since the used TPS5430 has a maximum input voltage of 36 V, and the desired negative output voltage is -13.5 V, the maximum input voltage would be 23.5 V. In order to avoid the maximum rating, the input voltage was set to 20V.

For the second stage, different Low-Dropout Regulators (LDO) from Texas Instruments were used for each voltage. LM3940 were used to obtain the 3.3 V to power the different ECT modules. The LM317 were used to achieve the 12 V, while the LM337-N the -12 V, both voltages are used on the ECT probes.

To accommodate the 4 front-end modules, probe connectors, power management circuitry and the processing core, a Printed Circuit Board (PCB) was design and produced. The software used was Altium Designer. Two layers were used to accommodate the required tracks. The power tracks have 1mm of width when possible since high current will flow through them. The signal tracks have 0.3mm of width. The connector pads are 1.5mm in diameter, with a hole size of 0.9mm to easily connect jumper wires to both program the front-end modules and check the different signal values. The probe connectors signal pads are 2mm in diameter with a 1.3mm hole, while the mounting pads are 3.5mm in diameter with a 2.4mm hole size. The power connector pad has 4mm in diameter with a hole size of 1.8mm. To attach the Beaglebone Black to the PCB pads with 3mm in diameter and a 2.5mm hole where also created. The clearance spacing between tracks and pads is 0.15mm to prevent any short circuit soldering the components. The components used are surface-mounted, to reduce the PCB footprint. The dimensions of the resistors and capacitors varies between 0603 and 1206 codes. When the capacitance was higher than 1 µF, 1206 components were used.

The Figure 10 represents a preview of the PCB layout based on the system architecture, that accommodates the 4 front-end modules, probe connectors, power management circuitry, as well as the processing core.

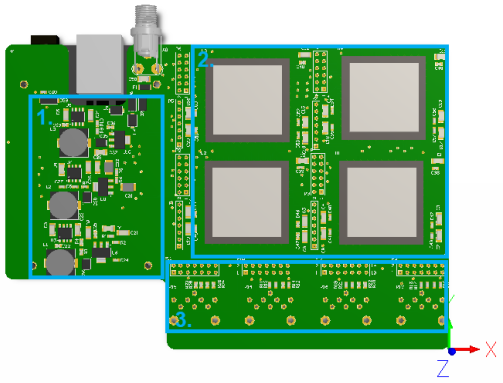

Figure 10 – Top PCB Layout.

The power management circuitry is located on the left side of the PCB, outlined by the section 1, along with the power connector. Over to the top left side of the PCB, is located the 4 front-end eddy current modules as well as the necessary connections to program the modules externally, delineated by the section 2. In the lower portion of the PCB are located the probe connectors inside section 3 of Figure

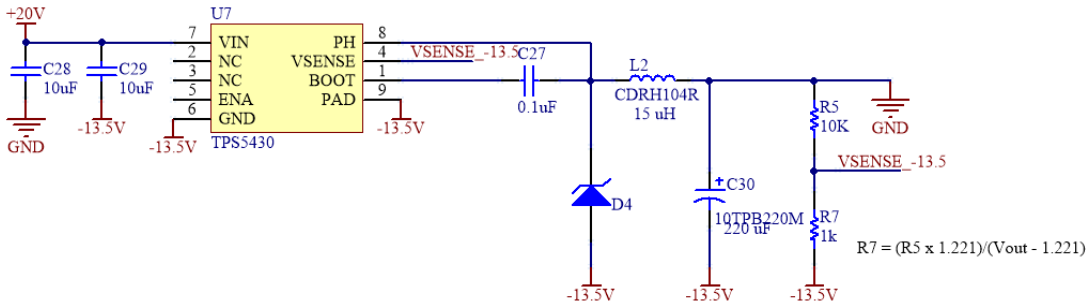

Figure 9 – Step-Down Converter Schematic for -13.5 V.

10. In between the modules and the probe connections, are pins to connect jumper wires to check the signal values if needed. Figure 11 and Figure 12 illustrates the prototype PCB where is possible to identify one ECT Front-End module, the required pins to debug and program the modules, some required circuitry and the processing core on the back side.

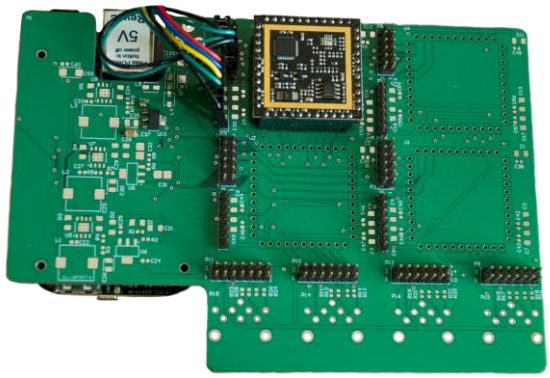

Figure 11 – Prototype PCB (Top View).

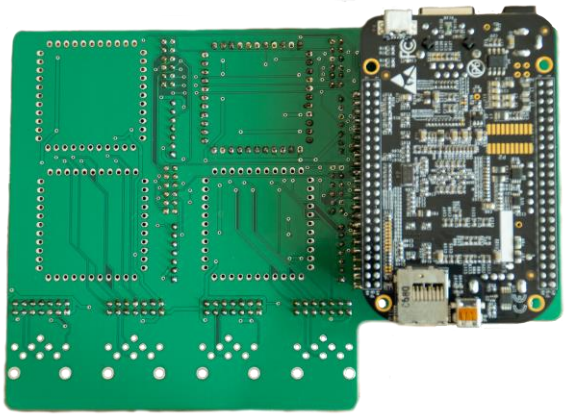

Figure 12 – Prototype PCB (Bottom View).

The eddy current front-end modules are powered by MSP430 FR2355 microcontrollers. To achieve the desired behavior, firmware was produced for these modules. The Beaglebone Black required some software development to communicate with the ECT modules. It also required to manipulate some key variables, such as the frequency at which the eddy current probes would operate and display the information on a user interface.

B. Software Architecture

The ECT modules implement four main functionalities: control and deliver the frequency signals to the eddy current probes, improve the ECT modules signal acquisition range using vector amplification, digitalize the probe readouts, and lastly communicate with the processing core.

In order to change frequencies with ease, the MSP430 uses one of the two available timers generate in-phase and quadrature digital waveforms needed for the hardware demodulator. These signals required to be in quadrature between one another, to accomplish this, the Timer_B is used and set to “Up Mode”. In this mode, the user defines a frequency value that translates to a certain timer increment value, obtained by

$$M = \frac{Clk}{2 * f}, \tag{14}$$

where Clk represents the clock at which the MSP is set to, and f the desired output frequency.

Each ECT front-end module is connected to one coil, the analog demodulator generates two DC signals corresponding to the real and imaginary components of the coil signal. To read that information separately, the 12-bit analog to digital converter present on the MSP430 FR2355 had to be configured in a way that was possible to capture both signals at the same time. To save the conversion values from the ADC, a temporary integer array is used. The converted readings are then stored in two distinct rotary buffers, one for the imaginary part, and one for the real part. These rotary buffers consist in two integer arrays with the capacity to store 64 values each.

Integrated Smart Analog Combos (SAC) were used. Each SAC is composed by a high-performance low-power operational amplifier, a programmable gain amplifier (PGA) and a 12-bit digital-to-analog (DAC) converter.

For both the imaginary and real parts of the signal, two SAC’s were used. One as an inverted, and the other as a DAC. The Figure 13 illustrates this configuration.

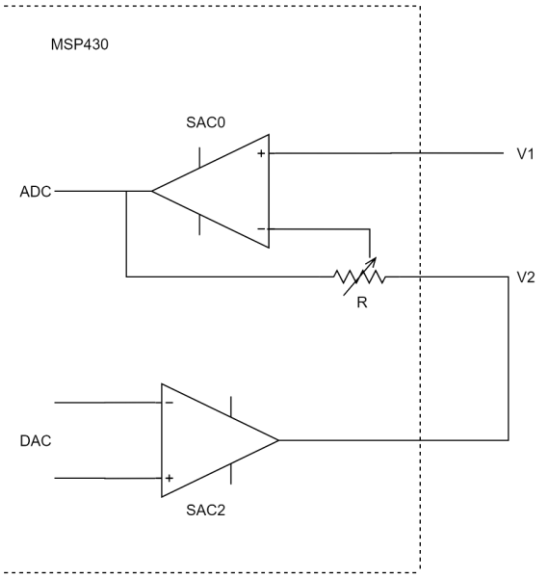

Figure 12 – MSP430 SAC's configuration.

The output of the SAC DAC (SAC2) is set with a compensation signal that connects to the negative input of the inverting amplifier SAC (SAC 0). The positive input of the SAC 0 is the post-demodulated DC component (real or imaginary) where the gain is regulated by the PGA integrated in the SAC. The readings from the SAC 0 are then used to change the calibration signal of the SAC DAC accordingly. The V_O can be calculated by

$$V_O = V_1(1 + \frac{R_2}{R_1}) - \frac{R_2}{R_1}V_2, \tag{22}$$

where $\frac{R_2}{R_1}$ represents the PGA gain, V_1 the probe readings signal and V_2 the calibration signal from the SAC DAC. Figure 12, $\frac{R_2}{R_1}$ is simplified to R.

Vector amplification is used to maximize the overall sensitivity. For this, a DC reference generated by the MSP430 FR2355 DAC are subtracted from the analog demodulator output. Programmable gain amplification is then applied before digitalizing using the MSP430 FR2355 internal ADC. A binary search function on the DAC output was developed so that the input signal on each of the ADC channels would be on the middle of the acquisition range. Has mentioned before, the MSP430 FR2355 has a 12-bit ADC, therefore, the reading range would be valued between 0x000 and 0xFFF, corresponding to 0 and 2.5V respectively. The best possible reading when no flaw is present is the middle of this range, 0x800. This is due to the fact that a flaw signal on eddy currents, normally translates into symmetrical real and imaginary trajectories. Therefore, if the readings when no flaw was present, are near one of the ADC limits, in a presence of a flaw, it may not be detected.

For the ECT modules to communicate with the processing core, SPI communication was used and configured. This communication protocol is used so that the Beaglebone Black can send and receive data, to and from the front-end modules, as well as change the eddy current testing parameters. The MSP430 was configured to use 8-bit data length, 4-pin SPI operation and set has a slave. The Beaglebone was configured the same way, with the only difference, it being set as the master. In order to change the configurations on the ECT modules, a control communication protocol was implemented. This protocol uses variable size commands that can include multiple parameters. The structure of a command is composed by four main sections as shown in Figure 13.

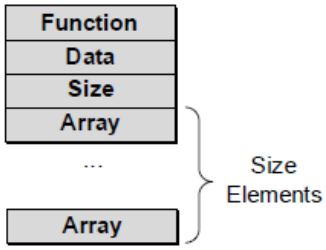

Figure 13 – MSP430 SAC's configuration.

Figure 13 – MSP430 SAC's configuration The Function defines the action or configuration to take or change; the Data is used when a single parameter is required; the Size is zero if no further data is required, otherwise carry the number of data elements to receive further; the Array has multiple parameters when required. The Table 5 includes some of the implemented commands. Both the Function and Size header fields are 32 bits wide, unsigned integers, big endian format. The Data field may use an integer or a floating point 32 bits wide number. The Array elements are 8 bits wide, raw data used to transmit any data format required.

A simple User Interface (UI) was developed using Python 3.4 and a Python plugin, PyQt, for the Graphical User Interface (GUI). The UI is capable of displaying and transmitting information to the processing core, which will communicate with the ECT Front-Ends using the developed communication protocol. Figure 14 ilustrates the developed UI, where is possible to input the frequency and amplitude of one channel. Over to the right side there is a graph that plots the combination introduced on the Real and Imaginary parts inputs. Idealy this graph would plot using the values aquired by the connected probes. There's also a button to call the developed binary search function that implements a vector amplification to the channel.

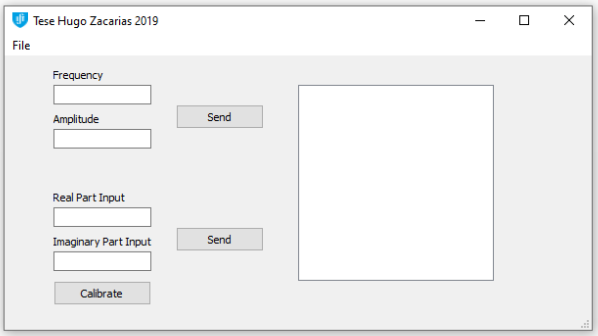

Figure 14 – Developed User Interface.

IV. Results and Conclusions

A. *Results*

The developed hardware and firmware were used to accomplish an operational ECT instrument while collaboration with the FCT-UNL NDT Laboratory. Some tests were carried on Unidirectional Carbon Fiber Reinforced Polymer Composites (UD CFRP) [33]. These are high performance materials for structural components that exhibit low damage tolerance. For that matter, condition monitoring is required for safety-critical applications. For these tests, the carbon fiber rope consists UD CFRP elements, protected by a polyurethane coating with an average thickness of 1 mm, a cross section dimension of roughly 5.0 × 2.5 mm and 100 mm length. The coil was placed 3 mm above the CFRP element, with an additional 2 mm lift-off distance to ensure contactless inspection. The effective lift-off distance is 3 mm due to the fact that the polyurethane coating is 1 mm thick. Different types of defects were induced in the test piece in order to represent natural imperfections or damages to the CFRP element. The ECT probe were coupled to a 3D printed handheld chassis with two wheels. The probes are attached to the middle of the chassis, assuring its constant positioning and lift-off distance along the test piece. The Figure 15 represents the mentioned chassis with the ECT probes attached. The CFRP serves as rails for the handheld chassis wheels roll on.

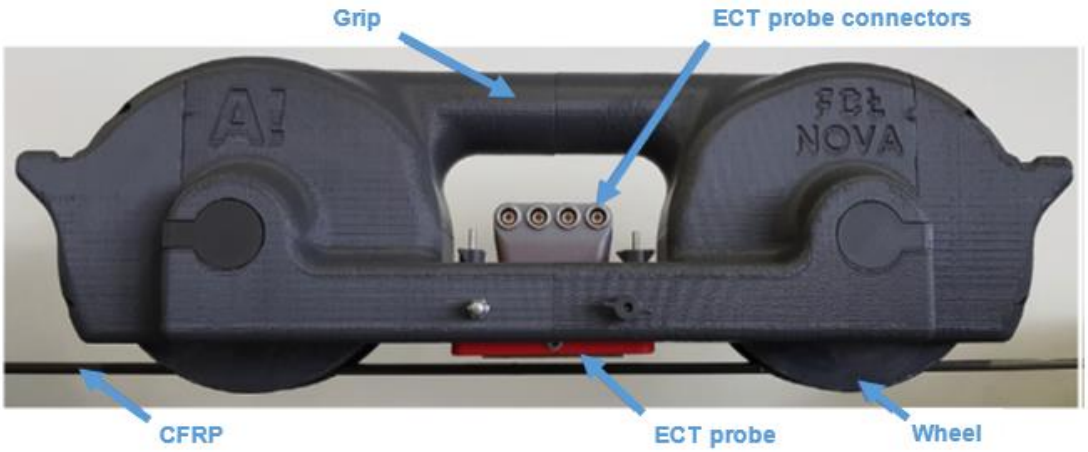

Figure 15 – Handheld device with the ECT probes.

Has previously mentioned, the test piece had different types of defects. Figure 16 and Figure 17 shows the output from the ECT probes connected to the developed ECT front-end at a speed of 3.5 m/s with a frequency of 1 MHz. Figure 16 represents the real part, whereas Figure 17 the imaginary part over time. The first and last differential signals were obtained by aluminium marks on the CFRP material to mark the beginning and ending of the inspection. The three indications shown in between where caused by the presence of three fiber break defects with different dimensions.

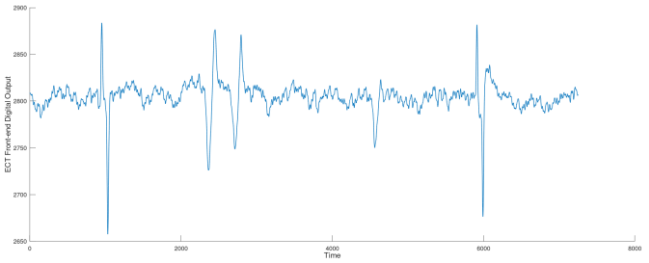

Figure 16 – Real part signal.

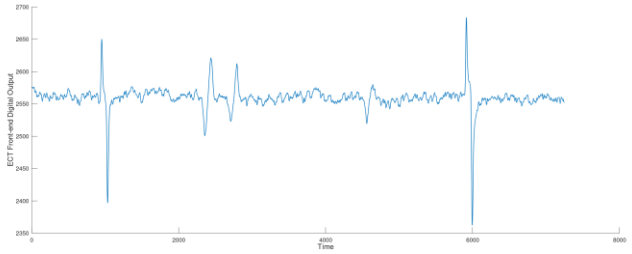

Figure 17 – Imaginary part signal.

B. Conclusions

Eddy current testing is one of the most used methods to inspect conductive materials, but its complexity requires a powerful processing unit. Remote access is an innovative step in the subject, as studies in this area tend to improve ECT efficiency. Incorporate Ethernet connection with an autonomous ECT instrument lead to a more convenient way for the user to access and share information, a key functionality in the present day.

This project presents a modular instrument capable of conducting multiple online eddy current inspections and detect the defects present in the test pieces. The instrument combines four ECT front end modules, each one connected to a probe, capable of analyze an independent eddy current field; a microcontroller Beaglebone Black to process the data sent by the ECT modules via SPI and provide remote access capabilities.

V. REFERENCES

[1] "Introduction to Nondestructive Testing." [Online]. Available: https://www.asnt.org/MinorSiteSections/AboutASNT/Intro-to-NDT.

[2] "History of Eddy Current Testing | Olympus IMS." [Online]. Available: https://www.olympus-ims.com/en/ndt-tutorials/eca-tutorial/intro/history/.

[3] Q. H. Nguyen, L. D. Philipp, D. J. Lynch, and A. F. Pardini, "Steam Tube Defect Characterization Using Eddy Current Z-Parameters," *Res. Nondestruct. Eval.*, vol. 10, no. 4, pp. 227–252, Jan. 1998.

[4] N. Rodrigues, L. Rosado, P. Ramos, "A Portable Embedded Contactless System for the Measurement of Metallic Material Conductivity and Lift-Off", Measurement, vol. 111, pp. 441-450, December 2017.

[5] P. Dominique and D. Isabelle, "Eddy current sensors for nondestructive inspection of graphite composite materials," *Conf. Rec. - IAS Annu. Meet. (IEEE Ind. Appl. Soc.*, vol. 1992–Janua, pp. 1676–1682, 1992.

[6] "Display - Complex Impedance Plane." [Online]. Available: https://www.nde-ed.org/EducationResources/CommunityCollege/EddyCurrents/Instrumentation/impedanceplane.htm.

[7] H. M. G. Ramos, O. Postolache, F. C. Alegria, and A. Lopes Ribeiro, "Using the skin effect to estimate cracks depths in mettalic structures," in 2009 IEEE Intrumentation and Measurement Technology Conference, 2009, pp. 1361–1366.

[8] "Penetration Depth & Reflectivity." [Online]. Available: https://slideplayer.com/slide/9395409/. [Accessed: 04-Jan-2019].

[9] A. Sophian, G. Y. Tian, D. Taylor, and J. Rudlin, "Electromagnetic and eddy current NDT in weld inspection: A review," Insight Non-Destructive Test. Cond. Monit., vol. 43, no. 5, pp. 302–306, 2001.

[10] K. A. Bartels and J. L. Fisher, "Multifrequency eddy current image processing techniques for nondestructive evaluation," in Proceedings., International Conference on Image Processing, vol. 1, pp. 486–489.

[11] "» Square Wave Calculations » Recordingology." [Online]. Available: http://recordingology.com/in-the-studio/distortion/square-wave-calculations/. [Accessed: 04-Jan-2019].

[12] R. Abrantes, L. Rosado, M. Piedade, P. Ramos, "Pulsed Eddy Current Testing using a Planar Matrix Probe", Measurement, Elsevier, vol. 77, pp. 351-361, January 2015.

[13] "MSP430FR4xx and MSP430FR2xx Family User's Guide", SLAU445H, 2014.